Preferential *c*-Axis Orientation of Ultrathin SnS$_2$ Nanoplates on Graphene as High-Performance Anode for Li-Ion Batteries

Shuangyu Liu, Xiang Lu, Jian Xie,* Gaoshao Cao, Tiejun Zhu, and Xinbing Zhao*

State Key Laboratory of Silicon Materials, Key Laboratory of Advanced Materials and Applications for Batteries of Zhejiang Province, and Department of Materials Science and Engineering, Zhejiang University, Hangzhou, 310027, China

Ⓢ *Supporting Information*

ABSTRACT: A SnS$_2$/graphene (SnS$_2$/G) hybrid was synthesized by a facile one-step solvothermal route using graphite oxide, sodium sulfide, and SnCl$_4$·5H$_2$O as the starting materials. The formation of SnS$_2$ and the reduction of graphite oxide occur simultaneously. Ultrathin SnS$_2$ nanoplates with a lateral size of 5−10 nm are anchored on graphene nanosheets with a preferential (001) orientation, forming a unique plate-on-sheet structure. The electrochemical tests showed that the nanohybrid exhibits a remarkably enhanced cycling stability and rate capability compared with bare SnS$_2$. The excellent electrochemical properties of SnS$_2$/G could be ascribed to the in situ introduced graphene matrix which offers two-dimensional conductive networks, disperses and immobilizes SnS$_2$ nanoplates, buffers the volume changes during cycling, and directs the growth of SnS$_2$ nanoplates with a favorable orientation.

KEYWORDS: graphene, tin sulfide, plate-on-sheet, c-axis orientation, Li-ion batteries, anode
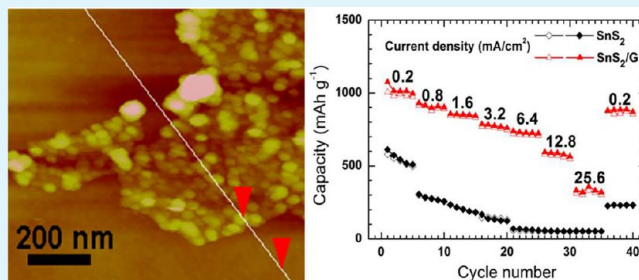
■ INTRODUCTION

Rechargeable Li-ion batteries (LIBs) are now considered as potential power sources for electric vehicles (EVs) and hybrid electronic vehicles (HEVs). In order to meet the increasing requirements for EVs and HEVs applications, an intensive research attention has been turned to design new electrode materials that bring high rate performance, cycling life, low cost, and enhanced safety for LIBs.[1−3] Among these materials, tin disulfides have received a particular interest as anode materials to replace the conventional carbon anodes for LIBs due to their high theoretical capacities.[4−6] The lithiation of SnS$_2$ obeys a two-step mechanism as: (1) SnS$_2$ + 4Li → Sn + 2Li$_2$S, and (2) Sn + xLi ↔ Li$_x$Sn ($x \leq 4.4$). The first step contributes to the first irreversible capacity, while the second step leads to a reversible theoretical capacity of 645 mAh g^{-1}, higher than that of commercial graphite anodes (theoretical value: 372 mA h g^{-1}). However, two critical problems limiting their practical applications could be the low first coulomb efficiency and the large volume expansion/contraction, resulting in loss of first capacity and rapid capacity fade upon cycling, respectively. The low first coulomb efficiency has been proved to be solvable by using Li-rich anodes, for example Li$_{2.6}$Co$_{0.4}$N.[7] Nevertheless, achieving long cycling life and good rate capability still remains a great challenge.

To achieve high reversible capacities and long cycling life at high current densities, the electrode material is generally required to possess high electrical conductivity and to maintain structural stability. For this purpose, great effort has been made to improve the electrochemical performance of SnS$_2$. A effective method to increase the electrical conductivity and structural

stability is to combine SnS$_2$ with a conducting matrix.[5,8,9] Fabricating nanostructured SnS$_2$, such as fullerene-like nanoparticles,[10] nanoflakes,[11] nanorods[12] and nanoplates[13] has been proved to be a practical strategy to improve the cycling stability and rate capability. However, to further improve high-rate cycling life for these nanostructured materials, a conductive matrix is indispensable to prevent agglomeration of nanoparticles and to supply conductive channels. The particles agglomeration will block the rapid Li-ion transport and reduce the utilization of active sites for Li storage. Graphene, a new two-dimensional (2D) carbon material, is considered as an ideal matrix to support nanoparticles due to its appealing characteristics such as large specific surface area,[14] superior electronic conductivity,[15] and excellent mechanical strength.[16] Recent research on some metal oxides,[17,18] Si,[19] and Sn[20,21] has shown that the electrochemical properties of these nanostructured anodes could be significantly enhanced by constructing hybrids with graphene. Similar to those of SnO$_2$,[17] the electrochemical properties of SnS$_2$ could also be obviously improved when forming SnS$_2$/graphene (SnS$_2$/G) nanohybrids.[22−24]

SnS$_2$ is a typical layered compound with a hexagonal symmetry. It can easily grow into 2D plate or sheet structure,[13] similar to cases in other layered metal disulfide.[25] For 2D plates or sheets, the grow direction on graphene matrix is a critical factor in determining the electrochemical properties. For SnS$_2$, the growth along *c*-axis direction on graphene is preferred in terms of the Li-intercalation kinetics since the electrochemical lithiation of SnS$_2$ generally starts with the intercalation of Li-ion
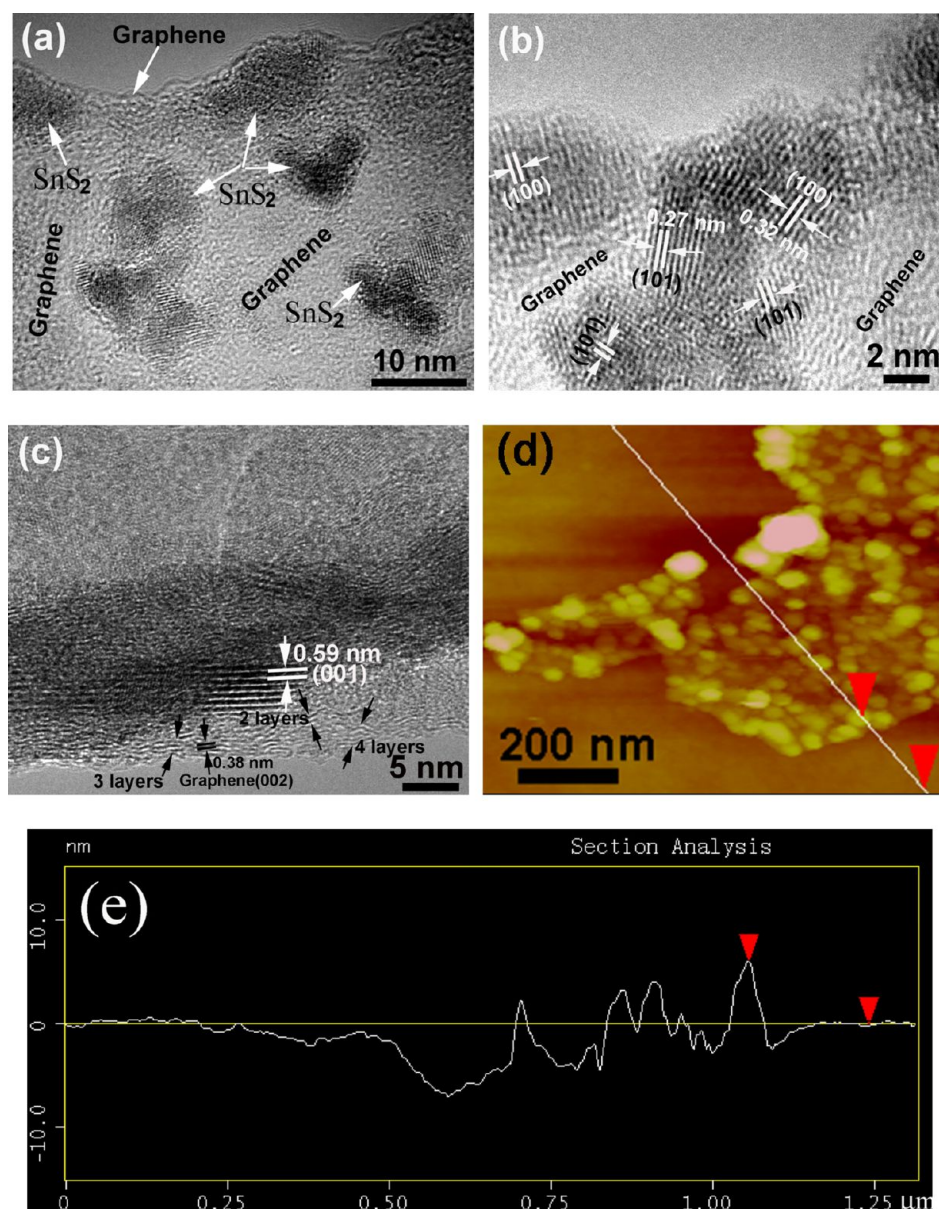
Figure 1. (a) TEM images, (b) HRTEM image of a planar sheet of SnS$_2$/G (c) HRTEM image of one stand-up sheet of SnS$_2$/G, (d) AFM image of SnS$_2$/G, and (e) height profile of SnS$_2$/G.

in between the (001) planes with large open edges.[13] This intercalation habit has been applied to prepare single- or few-layer sheet of metal disulfide using an electrochemical lithiation method.[26]

In this regard, it is favorable to prepare SnS$_2$ sheets or plates with (001) orientation on graphene. To our best knowledge, there is no report on the synthesis of SnS$_2$/G hybrid with (001) orientation of SnS$_2$ nanoplates on graphene. Herein, we report a facile solvothermal method to synthesize SnS$_2$ nanoplates anchored on conductive graphene as anode for high-performance LIBs. The SnS$_2$ nanoplates align on graphene with a (001) orientation. The SnS$_2$/G electrode can deliver a charge capacity of 303 mA h g^{-1} at 25.6 mA cm^{-2} (around 10 C) and maintain a charge capacity of 704 mA h g^{-1} after 100 cycles at 1.6 mA cm^{-2} (around 0.6 C). The origins of other attractive properties, such as the lower first irreversible capacity and higher reversible capacity (than the theoretical values) were also investigated by cycling the SnS$_2$/G electrode in a wide voltage range. The

results showed that the excellent electrochemical properties of SnS$_2$/G can be attributed to the combined buffering, conducting, and immobilizing effects of graphene, the synergistic effect between graphene nanosheets and SnS$_2$ nanoplates, and the preferential (001) orientation of SnS$_2$ nanoplates on graphene.

■ EXPERIMENT SECTION

Preparation of SnS$_2$/G Hybrid. Graphite oxide (GO, 50 mg), prepared by a modified Hummer's method,[27] was added into 50 mL of ethylene glycol (EG) with sonication to form a uniform dispersion. Then, 10 mL EG solution of SnCl$_4$·5H$_2$O (0.8 mmol) was added slowly to the above dispersion under stirring, followed by adding 10 mL of EG solution of Na$_2$S (1.6 mmol) dropwise. After vigorous stirring, the mixed dispersion was transferred to a 100 mL of Teflon-lined stainless steel autoclave and heated in an electric oven at 180 °C for 24 h. The resulting product was collected by centrifugation, washed with
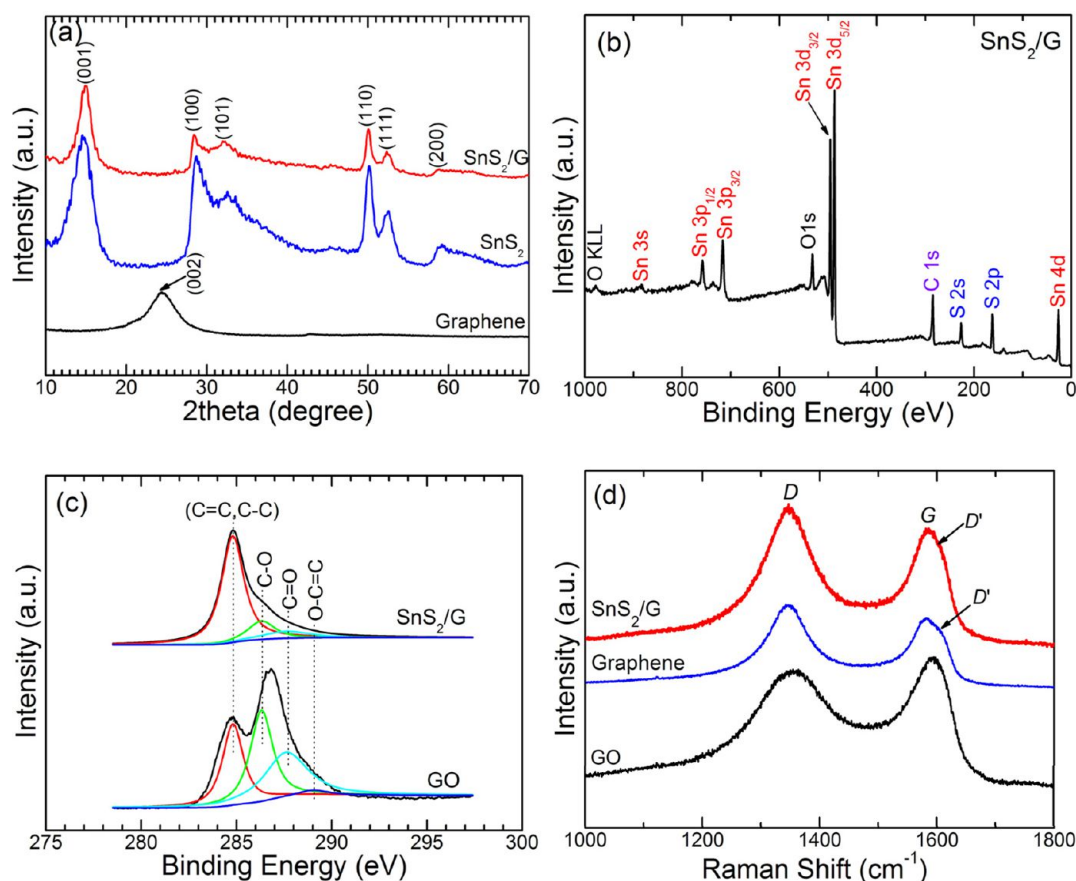
Figure 2. (a) XRD patterns of SnS$_2$/G, bare SnS$_2$ and graphene, (b) XPS survey spectrum of SnS$_2$/G, (c) C1s XPS of SnS$_2$/G and GO, and (d) Raman spectra of SnS$_2$/G, graphene and GO.

deionized water and absolute ethanol for several times and dried at 60 °C under vacuum for 8 h. A control experiment was carried out to prepare bare SnS$_2$ using the same route without adding GO. Bare graphene was also prepared using GO as the precursor with a similar route without adding SnCl$_4$·5H$_2$O and Na$_2$S.

Characterization. X-ray diffraction (XRD) patterns of the products were collected on a Rigaku D/Max-2550pc powder diffractometer equipped with Cu K$_\alpha$ radiation ($\lambda = 0.1541$ nm). X-ray photoelectron spectroscopy (XPS) analysis was performed on a KRATOS AXIS ULTRA-DLD spectrometer with a monochromatic Al K$_\alpha$ radiation ($h\upsilon = 1486.6$ eV). The morphologies and microstructures of the products were characterized by field emission scanning electron microscopy (FE-SEM) on a FEI-sirion microscope, transmission electron microscopy (TEM) on a JEM 2100F microscope, and atomic force microscopy (AFM) on a Vecco Multimode atomic force microscope using the tapping mode. The Raman spectra were measured on a Jobin-Yvon Labor Raman HR-800 using Ar-ion laser of 514.5 nm. Thermogravimetric (TG) analysis was conducted on a DSCQ1000 instrument from 30 to 500 °C at a heating rate of 10 °C min^{-1} in air.

Electrochemical Measurements. The electrochemical properties of the products were evaluated using CR2025-type coin cells. The working electrodes were made by spreading the slurry composed of 75 wt % active material (SnS$_2$/G or SnS$_2$), 15 wt % poly(vinylidene fluoride) (PVDF) and 10 wt % acetylene black on Ni foam current collector. The working electrodes were then dried at 100 °C under vacuum overnight.

The loading of active material is around 2 mg cm^{-2}. The electrodes were assembled into half cells in an Ar-filled glovebox using Li foil as the counter electrode and polypropylene microporous film (Celgard 2300) as the separator. The electrolyte used was 1 M LiPF$_6$ dissolved in ethylene carbonate (EC)/dimethyl carbonate (DMC) (1:1 in volume). The cells were charged at various current densities and discharged at 50 mA g^{-1} between 0.005 and 3 V vs Li/Li$^+$ on a Neware battery cycler (Shenzhen, China). The capacity of SnS$_2$/G was calculated based on the total mass of SnS$_2$ and graphene. Cyclic voltammetry (CV) experiments were conducted on an Arbin BT2000 system over the voltage range 0.005−3.0 V vs Li/Li$^+$ at 0.1 mV s^{-1}. All of the electrochemical measurements were performed at 25 °C.

■ RESULTS AND DISCUSSION

In situ solvothermal reactions using SnCl$_4$·5H$_2$O, Na$_2$S, and GO led to the formation of nanohybrid with the SnS$_2$ nanoplates uniformly decorated on graphene nanosheets as revealed by TEM and AFM observations (Figure 1). As seen in Figure 1a, SnS$_2$ nanoplates with a lateral size of 5−10 nm were firmly anchored on flat graphene even after a long time of vigorous ultrasonic treatment, suggesting strong interactions between the SnS$_2$ and graphene. It is believed that this plate-on-sheet structure is induced by the heterogeneous nucleation of SnS$_2$ on graphene.[28] Figure 1b shows the typical high-resolution TEM (HRTEM) images of a planar SnS$_2$/G sheet. The lattice spacings of 0.27 and 0.32 nm correspond to the (101) plane and (100) plane, respectively, of SnS$_2$. Figure 1c
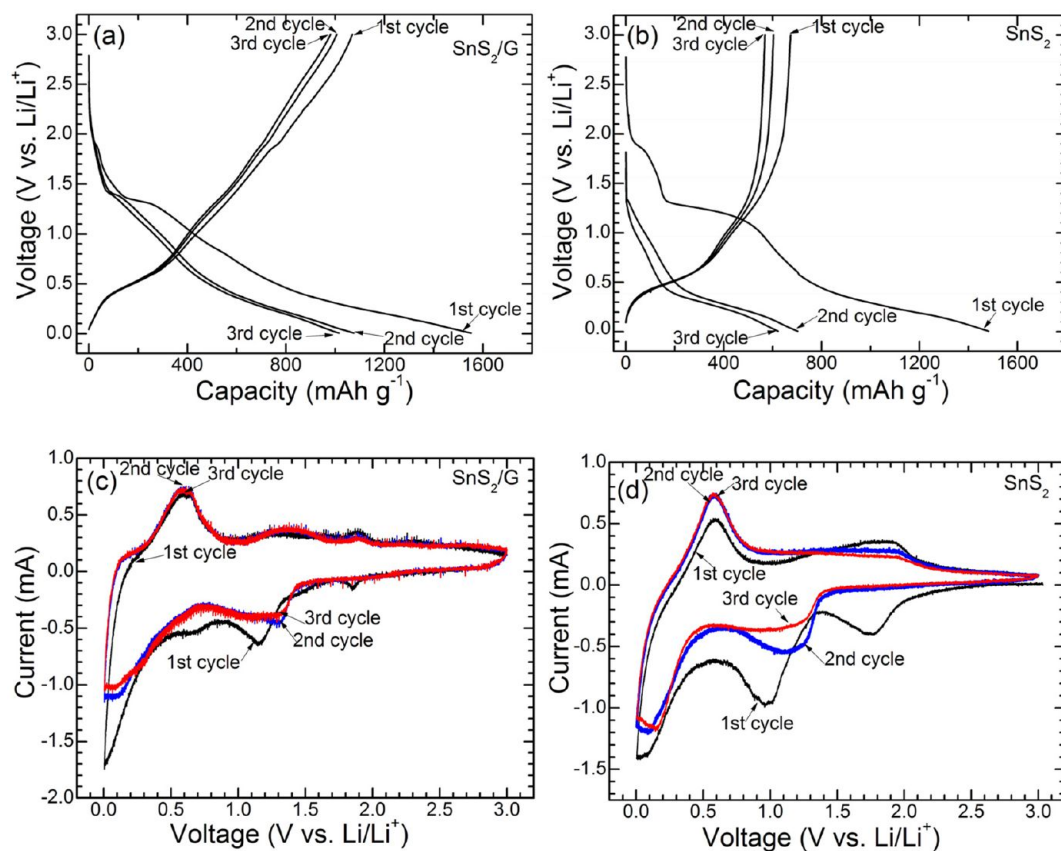
Figure 3. Voltage profiles of (a) SnS_2/G and (b) bare SnS_2 at a current density of 0.2 mA cm^{-2}, and CV plots of (c) SnS_2/G and (d) bare SnS_2 at a scan rate of 0.1 mV s^{-1} for the first three cycles.

shows the typical HRTEM images of a stand-up SnS_2/G sheet. The lattice spacing of 0.59 nm corresponds to the (001) plane of SnS_2 as denoted by the white arrows in Figure 1c. The cross-sectional TEM image indicates that the SnS_2 nanoplates align on graphene with c-axis orientation. The HRTEM images also confirm the few-layer feature of graphene as indicted by the black arrows in Figure 1c.

The formation mechanism of this preferential orientation can be attributed to the following factors: (1) GO is sufficiently exfoliated into graphene oxide sheets in EG by vigorous ultrasonic treatment; (2) Sn^{4+} ions are attracted onto the graphene oxide sheets by electrostatic force of the negatively charged graphene oxide;[29] (3) oriented alignment of SnS_2 nanoplates occurs spontaneously due to the confining effect of the restacked hydrophobic graphene sheets. This plate-on-sheet structure is expected to provide high accessibility to electrolyte and fast Li-ion transport pathways. AFM was also used to further investigate the structural details of the SnS_2/G hybrid (Figure 1d,e). From AFM height profile in Figure 1e, the thicknesses of SnS_2 plate and graphene sheet are estimated to be 2−5 nm and 1−2 nm, respectively, agreeing with the TEM observations. The AFM image also indicates that SnS_2 nanoplates are uniformly anchoring on graphene, consistent with the TEM results.

The crystal structure of SnS_2/G was analyzed by XRD. Figure 2a shows the XRD patterns of graphene, SnS_2 and $SnS_2/$ G. The graphene exhibits a broader diffraction peak (at about 24−28°) compared with perfectly crystallized natural graphite, which is possibly due to the short-range order in the stacked graphene sheets.[30] All of the diffraction peaks can be assigned

to the hexagonal SnS_2 (JCPDS Card no. 23−0677) for both SnS_2/G and bare SnS_2. The broad diffraction peaks of SnS_2 suggest the small size, agreeing with the TEM results. Interestingly, SnS_2 in SnS_2/G shows an obviously increased relative intensity of (001) peak to other peaks compared with bare SnS_2, indicative of a preferential c-axis orientation of SnS_2 plates on graphene, in consistent with the TEM results. The graphene content is estimated to be 30 wt % according to the TG analysis. However, at such a high content, the graphene diffraction peak (002 plane, generally at 24−28° 2θ)[31,32] cannot be detected in the hybrid, suggesting that the direct restacking of graphene sheets may be refrained by homogeneously loading SnS_2 nanoplates. The reduction of GO does occur evidenced from the presence of the (002) characteristic peak of graphene for bare graphene prepared by a similar route (Figure 2a).

The formation of SnS_2 and conversion of GO into graphene are further checked by XPS and Raman analyses. Figure 2b presents the XPS survey spectrum of SnS_2/G. The detected elements are Sn, S, C and O as expected for the SnS_2/G sample. The peaks at 487.1 and 495.6 eV correspond to the Sn3d$_{5/2}$ and Sn3d$_{3/2}$, respectively, of Sn^{4+} (see the Supporting Information, Figure S1).[33] The peaks at 25.5, 717.0, 759.4, and 884.6 eV are related to the Sn4d, Sn3p$_{3/2}$, Sn3p$_{1/2}$ and Sn3s bands, respectively.[34] The peak at 162.6 eV corresponds to S2p$_{3/2}$ in S_2^{2-}-like chemical state.[35] The C1s XPS of GO and SnS_2/G is given in Figure 2c. The spectra can be fitted into four peaks for carbon atoms in different functional groups: nonoxygenated carbon (C−C 285.6 eV or C=C, 284.8 eV), carbon in C−O bonds (286.3 eV), carbonyl carbon (C=O, 287.6 eV), and carboxylate carbon (O−C=O, 289. 0 eV).[36,37]

Note that the peak intensity of the oxygenated carbon shows a significant decrease after the solvothermal reactions, indicating a sufficient reduction of GO to graphene. The presence of O peaks and the C1s spectrum analysis also indicate that a small amount of oxygen-containing groups still exist, which possibly plays an important role in fixing and dispersing the SnS_2 nanoplates through chemical and/or physical absorption, even though they have a negative effect on the electronic conductivity of the hybrid.

The Raman spectra of GO, graphene, and SnS_2/G are shown in Figure 2d. In the Raman spectra of the three samples, two bands at 1350 and 1580 cm^{-1} appear, corresponding to the disordered (D) band and graphitic (G) band, respectively, of carbon-based materials.[38] Compared to GO, both SnS_2/G and graphene exhibit an increased D/G intensity ratio, caused by a reduction of the average size of the sp^2 domains, which can signify the reduction of GO to graphene.[36] Note that the G peak shows an asymmetric feature. In fact, the asymmetric peak is composed of two partly overlapped peaks, namely: the G and D' peaks. The D' peak at 1620 cm^{-1} is a defect peak due to intravalley scattering.[39] It could be concluded on the basis of the above analyses that a SnS_2/G nanohybrid has formed by this in situ one-pot solvothermal route.

To highlight the critical role that graphene plays in improving electrochemical properties of SnS_2, we compared the electrochemical properties of SnS_2/G and bare SnS_2. Figure 3a and 3b compare the voltage profiles between SnS_2/G and SnS_2 charged-discharged at 0.2 mA cm^{-2} (1/13 C) in the cutoff voltage 0.005−3.0 V vs Li/Li^+ . For simplicity, the C rates of both SnS_2 and SnS_2/G in this work are calculated based on theoretical capacity of SnS_2 (645 mA h g^{-1}) because it is difficult to obtain the exact theoretical capacity of SnS_2/G. The discharge is defined as the lithiation process of SnS_2 and graphene, that is: the formation of Li−Sn alloys (with Li_2S) and Li−C compounds (Li_xC), whereas charge is defined as the delithiation process of Li−Sn alloy and Li−C compounds. As shown in the figure, SnS_2/G yields the first charge and discharge capacities of 1070 and 1551 mA h g^{-1}, respectively, with the first irreversible loss of 31.0%, while the first charge and discharge capacities of bare SnS_2 are 673 and 1482 mA h g^{-1}, respectively, with the first irreversible loss of 54.5%. On the basis of the reactions

$$SnS_2 + 4Li \rightarrow Sn + 2Li_2S \tag{1}$$

$$Sn + 4.4Li \leftrightarrow Li_{4.4}Sn \tag{2}$$

the theoretical reversible capacity and the first irreversible loss of SnS_2 should be 645 mA h g^{-1} ($Li_{4.4}Sn$ composition) and 47.6% (Li_2S composition), respectively. It is clear that the introduction of graphene leads to an increase of the reversible capacity and a reduction of the first irreversible loss. For bare SnS_2, the additional first irreversible loss (besides the Li_2S formation) can be attributed to the formation of solid electrolyte interphase (SEI) layer, while for SnS_2/G, the irreversible loss related to the SEI formation is not significant.

As seen in Figure 3b, most of the charge capacity of bare SnS_2 is obtained in the voltage range of 0.005−1.5 V, where lithiation and delithiation of Sn occur.[40,41] The voltage increases rapidly above 1.5 V, which indicates that this voltage range only contributes to a small proportion of the total capacity and that the lithium in Li_2S is difficult to extract upon charging, similar to the case in SnO_2, where the formation of Li_2O during first discharge is also irreversible.[42] The voltage

profiles and the obtained capacity for bare SnS_2 confirm the above lithiation mechanism. For SnS_2/G, the theoretical capacity is estimated to be 540 mAh g^{-1} based on the theoretical capacity of SnS_2 and the content of graphene (30 wt %) and its yieldable capacity (around 300 mA h g^{-1}, see the Supporting Information, Figure S2). The extremely high capacity of SnS_2/G can be explained by the synergistic effect between SnS_2 and graphene. On one hand, the introduced graphene can uniformly disperse the SnS_2 nanoplates, max-imizing the exposure of the active material to the electrolyte and facilitating the rapid Li-ion transport across the electrode/electrolyte interface. On the other hand, the SnS_2 nanoplates can act as spacers to restrain the direct stacking of the graphene sheets, increasing the contact area of graphene with the electrolyte. In this case, the Li-ion storage in graphene also obeys an absorption mechanism in addition to the intercalation mechanism, similar to the case for nongraphitizable hard carbon.[43] In addition, the double-layer capacitance of graphene also contributes to the capacity above 0.5 V,[44] as evidenced by the sloping feature of the voltage profiles. This can explain the higher reversible capacity of SnS_2/G and the lower first irreversible capacity compared to their respective theoretical values.

To investigate the graphene on the electrode kinetics of SnS_2, CV measurements were performed. Figure 3c, d compare the CV plots of SnS_2/G and bare SnS_2 scanned at 0.1 mV s^{-1} between 0.005 and 3 V vs Li/Li^+. Three reduction peaks at 1.85, 1.28, and 0.65 V during the first scan are attributed to the decomposition of SnS_2 and the formation of Li_2S and Li−Sn alloys that may occur through a three-step process as suggested by Kim et al.[5] The oxidation peaks at 0.4−1.5 V correspond to the delithiation process upon charging. For SnS_2/G, a small peak at around 2.0 V may be related to partial decomposition of Li_2S, which also contributes to the rather high capacity and also the small first irreversible loss, while for bare SnS_2, the absence of this peak suggests that the Li_2S is totally electrochemically inactive. If Li_2S can be decomposed completely according to the reaction

$$SnS_2 + 8.4Li \leftrightarrow Li_{4.4}Sn + 2Li_2S \tag{3}$$
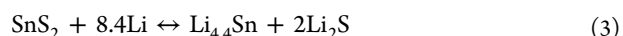
the theoretical capacity of SnS_2/G is estimated to be 952 mA h g^{-1}, close to its obtained value (1070 mAh g^{-1}) at low current density (0.2 mA cm^{-2}). Therefore, it is reasonable to expect that decomposition of Li_2S and recovery of SnS_2 is highly possible due to the high charge voltage (3.0 V), small size of SnS_2 crystals, and conductive effect of graphene. Nevertheless, the decomposition and recovery reactions may be only partial, considering the capacity contributed by absorbed Li ions and capacitance effect of graphene. Recent report has shown that SnO_2 can realize a fully reversible conversion when forming hybrid with single-walled carbon nanotubes (SWNTs) and conductive polypyrrole (PPy).[45] Similar high capacity was observed by Honma et al. when SnS_2/G was charged to 3.0 V.[24] After the first scan, the CV plots of SnS_2/G are almost overlapped, indicative of reversible electrochemical reactions (Figure 3c). In contrast, the peak intensity of bare SnS_2 is on the decrease with cycling (Figure 3d), indicating degraded electrode kinetics with cycling. The improved kinetics can be attributed to the electron storage properties of conductive graphene.[46] In addition, the (001) oriented SnS_2 plates on graphene also contributes to the enhanced electrode kinetics. On the basis of the above analyses, the lithiation and delithiation mechanism of SnS_2/G is proposed as shown in
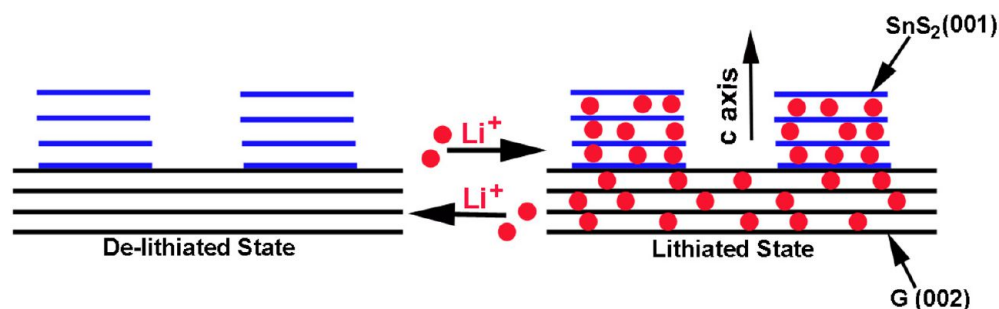
1592

dx.doi.org/10.1021/am302124f | ACS Appl. Mater. Interfaces 2013, 5, 1588−1595

Figure 4. Lithiation and delithiation mechanism of SnS_2/G.

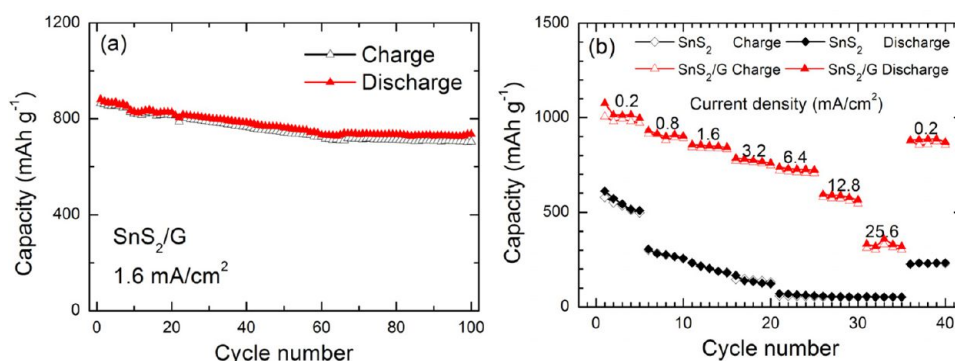**Figure 5.** (a) Cycling stability of SnS_2/G and capacity retention of the SnS_2/G charged at 1.6 mA cm^{-2} and discharged at 0.2 mA cm^{-2}, and (b) comparison of rate capability between SnS_2/G and bare SnS_2 charged at various current densities and discharged at 0.2 mA cm^{-2}.

Figure 4, where the actual lithiation/delithiation reactions is considered to be a combination of eqs 1−3.

Figure 5a shows the cycling stability of SnS_2/G charged at 1.6 mA cm^{-2} and discharged at 0.2 mA cm^{-2} for 100 cycles. Obviously, the SnS_2/G electrode exhibits high reversible capacity and excellent cycling stability. At a relatively high current density of 1.6 mA cm^{-2} (around 0.6 C), SnS_2/G can deliver an initial charge capacity as high as 864 mA h g^{-1}, while maintaining a charge capacity of 704 mA h g^{-1} in the 100th cycle, with a high capacity retention of 81%. For bare SnS_2, its charge capacity decreases rapidly from 674 to 217 mA h g^{-1} after 50 cycles at a low charge−discharge current of 0.2 mA cm^{-2} (see the Supporting Information, Figure S2). The enhanced cycling stability can be attributed to the in situ incorporated graphene that not only buffers the volume changes during the lithiation/delithiation reactions but also restrains the agglomeration of SnS_2 nanoplates upon long-term cycling. In addition, the absorption and trapping effects of graphene can suppress the dissolution of polysulfide, similar to the case for amorphous carbon.[47] Note that after 100 cycles, SnS_2 can still be attached on the graphene sheet (see the Supporting Information, Figure S3). The cycling stability of our SnS_2/G sample is higher than that measured at a smaller current density of 0.1 C.[24] For comparison, the cycling performance of bare graphene and the commercial natural graphite (the same sample used to make GO) is also presented (see the Supporting Information, Figure S2). The graphite electrode is charged at 1.6 mA cm^{-2} and discharged at 0.2 mA cm^{-2}. The natural graphite gives an initial charge capacity of only 315 mA h g^{-1}, much lower than that of SnS_2/G at the same current density. In addition, the cycling stability of SnS_2/G is comparable with that of the graphite sample. These results suggest that SnS_2/G shows a promising application as a high-capacity anode in LIBs.

The rate capability of SnS_2/G and SnS_2 is evaluated to further investigate the effect of graphene incorporation on the electrochemical performance of SnS_2 (Figure 5b). The samples were charged at various current densities and discharged at 0.2 mA cm^{-2}. It is obvious that the SnS_2/G hybrid displays a much better rate capability than bare SnS_2.When the current density reaches 12.8 mA cm^{-2}, the SnS_2/G electrode can still retain a charge capacity of 546 mA h g^{-1}. Even at a current density as high as 25.6 mA cm^{-2} (around 10 C), SnS_2/G still yields a charge capacity of 303 mA h g^{-1}. By contrast, the charge capacities of bare SnS_2 drop dramatically with increasing the current density. The results clearly demonstrate that the graphene plays an important role in improving the rate performance of SnS_2. It is believed that the enhanced rate capability originates from the three factors: first, the highly conductive graphene supplies 2D electronically conducting networks for the SnS_2/G nanoplates; second, ultrathin SnS_2 nanoplates with a preferential c-axis orientation are favorable for rapid Li-ion diffusion in bulk SnS_2 plates; third, the plate-on-sheet structure is beneficial for better wetting of the SnS_2/G hybrid and the rapid Li-ion transport across the electrode/electrolyte interface. Compared with the other SnS_2/G hybrids,[23,24] our SnS_2/G sample exhibits an improved rate capability under similar measurement conditions, possibly due to the preferential c-axis orientation of SnS_2 on graphene.

The lithiation−delithiation mechanism of SnS_2 was investigated by ex situ XRD upon first discharge−charge cycle as shown in Figure 6. Note that Sn, Li−Sn alloys and Li_2S phases form after first lithium addition. Meanwhile, the peak intensity of original SnS_2 is on the decrease during the discharge process, indicative of its decomposition upon Li uptake. When discharged to 0.005 V, the peaks of SnS_2 disappear with Sn, Li−Sn alloys and Li_2S phases formed. The small peaks at 2θ = 20−26° are related to the various Li−Sn phases (Li_5Sn_2,

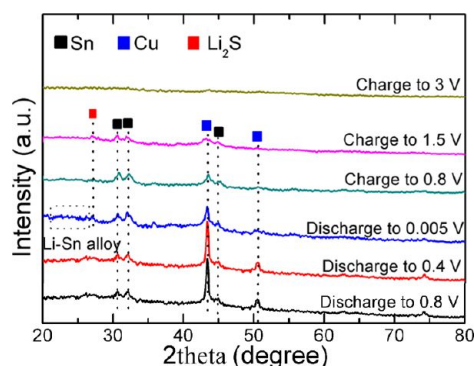**Figure 6.** Ex situ XRD of SnS$_2$/G electrode at different charge−discharge states.

Li$_{13}$Sn$_5$, Li$_7$Sn$_2$, Li$_{22}$Sn$_5$).[42] The presence of Sn at this potential indicates that the lithiation reactions of Sn cannot be fully completed even though at deep discharge state. When recharged to 0.8 V, Li−Sn alloys phases disappeared completely, indicating the decomposition of these phases upon Li-extraction, At the charge potential of 3 V, all the diffraction peaks disappear, indicating that the delithiated products show a poor crystallization.

CONCLUSIONS

Ultrathin SnS$_2$ nanoplates grow with a preferential c-axis orientation on graphene via a facile solvothermal process. The thicknesses of the SnS$_2$ plate and the graphene sheet are measured to be 2−5 nm and 1−2 nm, respectively. The SnS$_2$/G nanohybrid exhibits an improved cycling stability compared to bare SnS$_2$ due to the effective buffering and immobilizing effects of graphene. After 100 cycles at 1.6 mA cm^{-2} (around 0.6 C), a charge capacity of 704 mA h g^{-1} can be maintained. The unique plate-on-sheet structure not only offers 2D conducting networks but also facilitates the rapid Li-ion transport, leading to enhanced rate capability. The preferential c-axis orientation of the SnS$_2$ nanoplates on graphene also contributes to the excellent rate capability. At a current density up to 25.6 mA cm^{-2} (around 10 C), SnS$_2$/G can still yield a charge capacity of 303 mA h g^{-1}. Because of the synergistic effect between SnS$_2$ and graphene, the hybrid also exhibits a smaller first irreversible capacity and a higher reversible capacity compared with the theoretical values. The excellent electrochemical performance of SnS$_2$/G makes it a promising anode for LIBs.

ASSOCIATED CONTENT

Ⓢ Supporting Information

Sn 3d XPS of the SnS$_2$/G hybrid, cycling stability of bare SnS$_2$, natural graphite and graphene, and TEM images of SnS$_2$/G after 100 cycles. This material is available free of charge via the Internet at http://pubs.acs.org/.

AUTHOR INFORMATION

Corresponding Author

*E-mail: xiejian1977@zju.edu.cn (J.X.); zhaoxb@zju.edu.cn (X.Z.). Tel: +86 571 87951451. Fax: +86 571 87951451.

Notes

The authors declare no competing financial interest.

REFERENCES

(1) Poizot, P.; Laruelle, S.; Grugeon, S.; Dupont, L.; Tarascon, J. M. Nature 2000, 407, 496−499.
(2) Tarascon, J. M.; Armand, M. Nature 2001, 414, 359−367.
(3) Cabana, J.; Monconduit, L.; Larcher, D.; Palacín, M. R. Adv. Mater. 2010, 22, E170−E192.
(4) Kim, H. S.; Chung, Y. H.; Kang, S. H.; Sung, Y. E. Electrochim. Acta 2009, 54, 3606−3610.
(5) Kim, T. J.; Kim, C. J.; Son, D.; Choi, M.; Park, B. J. Power Sources 2007, 167, 529−535.
(6) Zhai, C. X.; Du, N.; Zhang, H.; Yang, D. R. Chem. Commun. 2011, 47, 1270−1272.
(7) Yang, J.; Takeda, Y.; Imanishi, N.; Yamamoto, O. J. Electrochem. Soc. 2000, 147, 1671−1676.
(8) Aswanni, Y.; Enrico, M.; Helen, A. T.; Martin, P.; Ute, K.; Wolfgang, T. Chem. Mater. 2009, 21, 2474−2481.
(9) Zhai, C. X.; Du, N.; Zhang, H.; Yu, J. X.; Yang, D. R. ACS Appl. Mater. Interfaces 2011, 3, 4067−4074.
(10) Hong, S. Y.; Biro, R. P.; Prior, Y.; Tenne, R. J. Am. Chem. Soc. 2003, 125, 10470−10474.
(11) Chen, D.; Shen, G. Z.; Tang, K. B.; Lei, S. J.; Zheng, H. G.; Qian, Y. T. J. Cryst. Growth 2004, 260, 469−474.
(12) Wu, P.; Du, N.; Zhang, H.; Liu, J.; Chang, L. T.; Wang, L.; Yang, D. R.; Jiang, J. Z. Nanoscale 2012, 4, 4002−4006.
(13) Seo, J. W.; Jang, J .T.; Paik, S. W.; Kim, C.; Park, B.; Cheon, J. Adv. Mater. 2008, 20, 4269−4273.
(14) Stoller, M. D.; Park, S. J.; Zhu, Y. W.; An, J. H.; Ruoff, R. S. Nano Lett. 2008, 8, 3498−3502.
(15) Park, S. J.; An, J. H.; Jung, I. H.; Piner, R. D.; An, S. J.; Li, X. S.; Velamakanni, A.; Ruoff, R. S. Nano Lett. 2009, 9, 1593−1597.
(16) Lee, C. G.; Wei, X. D.; Kysar, J. W.; Hone, J. Science 2008, 321, 385−388.
(17) Wu, Z. S.; Zhou, G. M.; Yin, L. C.; Ren, W. C.; Li, F.; Cheng, H. M. Nano Energy 2012, 1, 107−131.
(18) Zhou, W. W.; Zhu, J. X.; Cheng, C. W.; Liu, J. P.; Yang, H. P.; Cong, C. X.; Guan, C.; Jia, X. T.; Fan, H. J.; Yan, Q. Y.; Li, C. M.; Yu, T. Energy Environ. Sci. 2011, 4, 4954−4961.
(19) Su, L. W.; Jing, Y.; Zhou, Z. Nanoscale 2011, 3, 3967−3983.
(20) Wang, G. X.; Wang, B.; Wang, X. L.; Park, J.; Dou, S. X.; Ahn, H.; Kim, K. J. Mater. Chem. 2009, 19, 8378−8384.
(21) Ji, L. W.; Tan, Z. K.; Kuykendall, T.; An, E. J.; Fu, Y. B.; Battaglia, V.; Zhang, Y. G. Energy Environ. Sci. 2011, 4, 3611−3616.
(22) Chang, K.; Wang, Z.; Huang, G. C.; Li, H.; Chen, W. X.; Lee, J. Y. J. Power Sources 2012, 201, 259−266.
(23) Zhuo, L. H.; Wu, Y. Q.; Wang, L. Y.; Yu, Y. C.; Zhang, X. B.; Zhao, F. Y. RSC Adv. 2012, 2, 5084−5087.
(24) Sathish, M.; Mitani, S.; Tomai, T.; Honma, I. J. Phys. Chem. C 2012, 116, 12475−12481.
(25) Coleman, J. N.; Lotya, M.; O'Neill, A.; Bergin, S. D.; King, P. J.; Khan, U.; Young, K.; Gaucher, A.; De, S.; Smith, R. J.; Shvets, I. V.; Arora, S. K.; Stanton, G.; Kim, H. Y.; Lee, K.; Kim, G. T.; Duesberg, G. S.; Hallam, T.; Boland, J. J.; Wang, J. J.; Donegan, J. F.; Grunlan, J. C.; Moriarty, G.; Shmeliov, A.; Nicholls, R. J.; Perkins, J. M.; Grieveson, E. M.; Theuwissen, K.; McComb, D. W.; Nellist, P. D.; Nicolosi, V. Science 2011, 331, 568−571.

(26) Wu, S. X.; Zeng, Z. Y.; He, Q. Y.; Wang, Z. J.; Wang, S. J.; Du, Y. P.; Yin, Z. Y.; Sun, X. P.; Chen, W.; Zhang, H. *Small* **2012**, *8*, 2264−2270.

(27) Hummers, W. S.; Offeman, R. E. *J. Am. Chem. Soc.* **1958**, *80*, 1339−1339.

(28) Zhu, J. X.; Zhu, T.; Zhou, X. Z.; Zhang, Y. Y.; Lou, X. W.; Chen, X. D.; Zhang, H.; Hng, H. H.; Yan, Q. Y. *Nanoscale* **2011**, *3*, 1084−1089.

(29) Li, D.; Muller, M. B.; Gilje, S.; Kaner, R. B.; Wallace, G. G. *Nat. Nanotechnol.* **2008**, *3*, 101−105.

(30) Si, Y. C.; Samulski, E. T. *Chem. Mater.* **2008**, *20*, 6792−6797.

(31) Wang, G. X.; Yang, J.; Park, J.; Gou, X. L.; Wang, B.; Liu, H.; Yao, J. *J. Phys. Chem. C* **2008**, *112*, 8192−8195.

(32) Tang, L. H.; Wang, Y.; Li, Y. M.; Feng, H. B.; Lu, J.; Li, J. H. *Adv. Funct. Mater.* **2009**, *19*, 2782−2789.

(33) Lei, Y. Q.; Song, S. Y.; Fan, W. Q.; Xing, Y.; Zhang, H. J. *J. Phys. Chem. C* **2009**, *113*, 1280−1285.

(34) Ma, D. K.; Zhou, H. Y.; Zhang, J. H.; Qian, Y. T. *Mater. Chem. Phys.* **2008**, *111*, 391−395.

(35) Zhu, L.; Susac, D.; Teo, M.; Wong, K. C.; Wong, P. C.; Parsons, R. R.; Bizzotto, D.; Mitchell, K. A. R.; Campbell, S. A. *J. Catal.* **2008**, *258*, 35−242.

(36) Stankovich, S.; Dikin, D. A.; Piner, R. D.; Kohlhaas, K. A.; Kleinhammes, A.; Jia, Y. Y.; Wu, Y.; Nguyen, S. T.; Ruoff, R. S. *Carbon* **2007**, *45*, 1558−1565.

(37) Shin, H. J.; Kim, K. K.; Benayad, A.; Yoon, S. M.; Park, H. K.; Jung, I. S.; Jin, M. H.; Jeong, H. K.; Kim, J. M.; Choi, J. Y.; Lee, Y. H. *Adv. Funct. Mater.* **2009**, *19*, 1987−1992.

(38) Tuinstra, F.; Koenig, J. L. *J. Chem. Phys.* **1970**, *53*, 1126−1130.

(39) Ferrari, A. C. *Solid State Commun.* **2007**, *143*, 47−57.

(40) Huggins, R. A. *J. Power Sources* **1999**, *81−82*, 13−19.

(41) Zhang, R. G.; Upreti, S.; Whittingham, M. S. *J. Electrochem. Soc.* **2011**, *158*, A1498−A1504.

(42) Courtney, I. A.; Dahn, J. R. *J. Electrochem. Soc.* **1997**, *144*, 2045−2052.

(43) Dahn, J. R.; Zheng, T.; Liu, Y. H.; Xue, J. S. *Science* **1995**, *270*, 590−593.

(44) Yoo, E.; Kim, J.; Hosono, E.; Zhou, H. S.; Kudo, T.; Honma, I. *Nano Lett.* **2008**, *8*, 2277−2282.

(45) Zhao, Y.; Li, J. X.; Wang, N.; Wu, C. X.; Dong, G. F.; Guan, L. H. *J. Phys. Chem. C* **2012**, *116*, 18612−18617.

(46) Radich, J. G.; Kamat, P. V. *ACS Catal.* **2012**, *2*, 807−816.

(47) Shi, W. H.; Zhu, J. X.; Rui, X. H.; Cao, X. H.; Chen, C.; Zhuang, H.; Hng, H. H.; Yan, Q. Y. *ACS Appl. Mater. Interfaces* **2012**, *4*, 2999−3006.

1595

dx.doi.org/10.1021/am302124f | *ACS Appl. Mater. Interfaces* 2013, 5, 1588−1595